

Simulated Response of MuTe, a Hybrid Muon Telescope

A. Vásquez-Ramírez,^a M. Suárez-Durán,^b A. Jaimes-Motta,^a R. Calderón-Ardila,^{c,d} J. Peña-Rodríguez,^a J. Sánchez-Villafrades,^e J.D. Sanabria-Gómez,^a H. Asorey,^{c,f,g} and L.A. Núñez.^{a,h} on behalf of MuTe collaboration

^a*Escuela de Física, Universidad Industrial de Santander,
Bucaramanga, Colombia*

^b*Departamento de Física y Geología, Universidad de Pamplona,
Pamplona, Colombia*

^c*Instituto de Tecnologías en Detección y Astropartículas, Centro Atómico Constituyentes, Comisión Nacional de Energía Atómica,
Buenos Aires, Argentina*

^d*Universidad Nacional de San Martín, Instituto SABATO,
Argentina*

^e*Escuela de Ingeniería Eléctrica, Electrónica y de Telecomunicaciones, Universidad Industrial de Santander,
Bucaramanga, Colombia*

^f*Centro Atómico Bariloche, Comisión Nacional de Energía Atómica,
San Carlos de Bariloche, Argentina*

^g*Escuela de Producción, Tecnología y Medio Ambiente, Universidad Nacional de Río Negro,
San Carlos de Bariloche, Argentina*

^h*Departamento de Física, Universidad de Los Andes,
Mérida, Venezuela*

E-mail: adrianacvr67@gmail.com

ABSTRACT: In this paper we present a complete and detailed computational model of the response of the hybrid Muon Telescope (*MuTe*), designed to perform muography volcanic studies. This instrument combines two particle detection techniques: first, a muon hodoscope based on two panels of plastic scintillator bars; and a Water Cherenkov detector located behind the rear scintillator panel acting both as a coincidence and a discriminating detector. The simulation model includes: materials, geometries, dimensions, and the photo-sensitiveness of the detectors; as well as its response to the expected muon flux at 2650 m a.s.l at Cerro Machín Volcano, Colombia. The results obtained, in agreement with several experimental setups, were used to set up the muon detector trigger for the expected energy dependent signal.

KEYWORDS: Detector modelling and simulations I, Hybrid detectors, Scintillators, Cherenkov and transition radiation.

ARXIV EPRINT: [1912.10081](https://arxiv.org/abs/1912.10081)

¹Corresponding author.

Contents

1	Introduction	1
2	The MuTe instrumental design	2
3	Hodoscope response to cosmic ray background	3
3.1	The scintillator bar model	4
3.1.1	Attenuation of the photons in the <i>Bar-Fiber-SiPM</i> system	6
3.1.2	SiPM and fiber coupling	8
3.2	Experimental results from the scintillator detector	8
3.2.1	Dependence of the breakdown voltage with temperature	9
3.2.2	Attenuation measurements of the <i>Bar-Fiber-SiPM</i> system	9
3.3	Simulated attenuation in the hodoscope	11
4	The water Cherenkov detector response to cosmic background radiation	12
4.1	Estimation of the Vertical Equivalent Muon unit	13
4.2	WCD response to the cosmic ray background radiation	14
5	Conclusions	15

1 Introduction

Cosmic rays (*CR*) are continuously impinging the Earth's atmosphere producing cascades of secondary particles called extensive air showers (*EAS*), having three main components: the electromagnetic, the hadronic, and the muonic. The electromagnetic component produced by electrons, positrons, and photons, coupled through several processes. The hadronic component generated by barions and mesons produced through QCD interactions, and the muonic component, caused mainly of muons coming from the decay of charged pions, kaons, and other charged mesons through weak interactions processes. The energy of these muons comprises a broad spectrum, but only those muons with the highest energies ($> 1\text{TeV}$) –produced during the very first interactions of the evolving particles cascade– such as the decay of charmed mesons, are collectively known as prompt muons and have enough energy to cross from hundreds to thousand meters of rock [1].

Muography is an emerging technique based on measuring the attenuation of the directional muon flux moving across geological or anthropic structures [2]. Nowadays we are witnessing several new successful academic and commercial applications such as the detection of hidden materials in containers [3], archaeological building scanning [4, 5], nuclear plant inspection [6], nuclear waste monitoring, underground cavities [7], the overburden of railway tunnels [8] and vulcanology applications (see, e.g., [9] and references therein). The existence of more than a dozen active volcanoes in Colombia, which represents significant risks to the nearby population [10–12],

motivated local research groups to explore possible applications of the muography technique [13–18].

Hodoscopes are the most common detectors designed and used for volcano muography and consist of two or more panels devised to identify muon trajectories. Projects like *MU-RAY* [19], *ToMuVol* [20], and *DIAPHANE* [21] use hodoscopes based on different detection technologies: emulsion plates, resistive plate chambers, micromegas, multi-wire proportional cameras, and scintillators, just to mention the most common ones. Each of these techniques has advantages and disadvantages: Emulsion plate detectors [4, 22] provide an excellent spatial resolution of the order of sub-microns, are passive, and easy to handle. On the other hand, they have short lifetimes, and it is not possible to discriminate the time-stamp of dynamic phenomena, because the recorded events accumulate in the plates. Gas detectors, as Resistive Plate Chambers [23, 24], Micromegas [25], and Multi-Wire Proportional Cameras [26], makes possible the capture of the short traces due to the detected particles with microns resolution. However, for such a low muon flux, it is difficult to address the benefits of this high spatial resolution fully and, since these detectors operate outdoors, environmental temperature fluctuations could affect the detector operation. Finally, scintillation based detectors, using segmented [6, 27, 28] or continuous scintillators [29–31] – which does not experience considerable mechanical variation caused by environmental conditions– are more robust and more affordable than gaseous and emulsion detectors. Nevertheless, their spatial resolution is not as good as the above mentioned detectors since the segments generally used are of the order of centimeters.

In this paper, we present a detailed computational *Geant4* model of our hybrid Muon Telescope (*MuTe*) and the estimation of its response for an expected atmospheric muon flux at 2650 m a.s.l at Cerro Machín Volcano-Colombia. *MuTe* combines two detection techniques: a hodoscope with two detection planes of plastic scintillator bars, and a Water Cherenkov Detector (*WCD*) which acts as an absorbing element and as a third active coincidence detector. The model includes materials, detailed geometries and dimensions, and the detector’s photo-sensitive devices. In the next section, we briefly describe the rationale behind the *MuTe* design. Section 3 discussed the response from scintillator bar hodoscope to the impinging cosmic ray background. We emphasize in the bar scintillator model and the possible attenuation effects. In section 3.2, we compare our simulation results with data obtained from an experimental laboratory setup and examine the relationship between temperature and the breakdown voltage of the silicon photo-multiplier (*SiPM*) used in the scintillator panels. Section 4 presents the response of the *WCD* and compares some of the results with recent lab measurements. Finally in section 5 we summarize some final remarks and conclusions.

2 The *MuTe* instrumental design

As we have mentioned above, our Muon Telescope (sketched in figure 1) is a hybrid detector that combines two technologies: a two-panel scintillator bar hodoscope, and a water Cherenkov detector, increasing the signal/noise ratio and minimizing the backward noise [32–35]. This hybrid technique allows us to estimate not only the incoming flux directions but also the range of energy deposited by the impinging particles [13, 18].

The panels of the hodoscope consist of an array of 30 vertical \times 30 horizontal scintillator bars, with dimensions $(4\text{cm} \times 1\text{cm} \times 120\text{cm})$ long, providing 900 pixels of $4\text{cm} \times 4\text{cm}$, and a total detection surface of 14.400cm^2 . Scintillation bars are made of StyronTM 665-W polystyrene doped with a mixture of liquid organic scintillators: 1% of 2,5-diphenyloxazole (PPO) and 0.03% of 1,4-bis (5-phenyloxazol-2-yl) benzene (POPOP) [36], having a photon emission peak at the wavelength of 420 nm. Each bar has a 0.25 mm highly reflective coat made of 85% Polystyrene and 15% of TiO_2 . At the center, each bar has a $\sim 3\text{mm}$ diameter hole longitudinally drilled, where a 1 mm, wavelength shifter (WLS) and multi-cladded optical fiber (Saint Gobain BCF92) is placed. The fiber core is made of Polymethyl methacrylate, with the inner cladding of Polyethylene, and the external one of Fluorinated Polyethylene [37]. Scintillation photons produced by the passage of charged particles through the bars are partially collected by the fiber, absorbed, and re-emitted in a different wavelength and transported along the fiber. One extreme of the fiber is polished at an angle of 45 degrees to increase internal reflection and to favor photon collection in the opposite end. Mechanically coupled to the fiber, is a silicon photomultiplier (Hamamatsu S13360-1350CS), which has a photosensitive surface of $1.3\text{ mm} \times 1.3\text{ mm}$, consisting of 2668 avalanche photodiodes [38]. This device has a spectral detection range from 270 to 900nm, with its maximum sensitivity around 450nm.

Casual coincidences detection and discrimination of the muon signals from background noise are enhanced by using our in-house developed Time-of-Flight (*ToF*) recording system, complemented by a cubic 120 cm side water Cherenkov detector (see figure 1). The *WCD* consists of a cubic stainless steel container, internally coated with a reflective and diffusive material (0.4 mm Tyvek [39]) and filled with 1.7 m^3 of purified water, having an 8" Hamamatsu R5912 photomultiplier tube (*PMT*) placed at the center of the tank roof. In this way, the photosensitive *PMT* window is in direct contact with the water and can detect Cherenkov photons produced by relativistic charged particles moving through the detector (see figure 1).

This particular design filters the soft-component (e^\pm) of Extensive Air Showers and scattered/upward-coming muons. The energy deposited by particles in the *WCD* identifies the electron/positron component, while scattered and backward muons are rejected using a pico-second *ToF* system.

3 Hodoscope response to cosmic ray background

The response of the hodoscope bars refers to the signal produced in the *SiPM* photo-sensor when a charged particle crosses each scintillator bar. Indirect detection of secondary *EAS* photons is also possible mainly through Compton scattering and even pair creation. However, as the scintillation detector volume is relatively small, these mechanisms are highly improbable.

As shown in figure 2, charged particles impinging the scintillators produce photons in the blue-violet-ultra violet bands, which can be absorbed by the plastic material or collected by the *WLS* fiber. The fiber cladding helps to capture photons, conduct them through the fiber where they can be absorbed, re-emitted –in the green optical band– and guided to the photo-sensor device located at one of the extremes of the fiber [37].

In the following sections we shall discuss the *Geant4* [40] bar simulation model, the experimental setup to validate them (see section 3.2) and the estimation of the average response of the

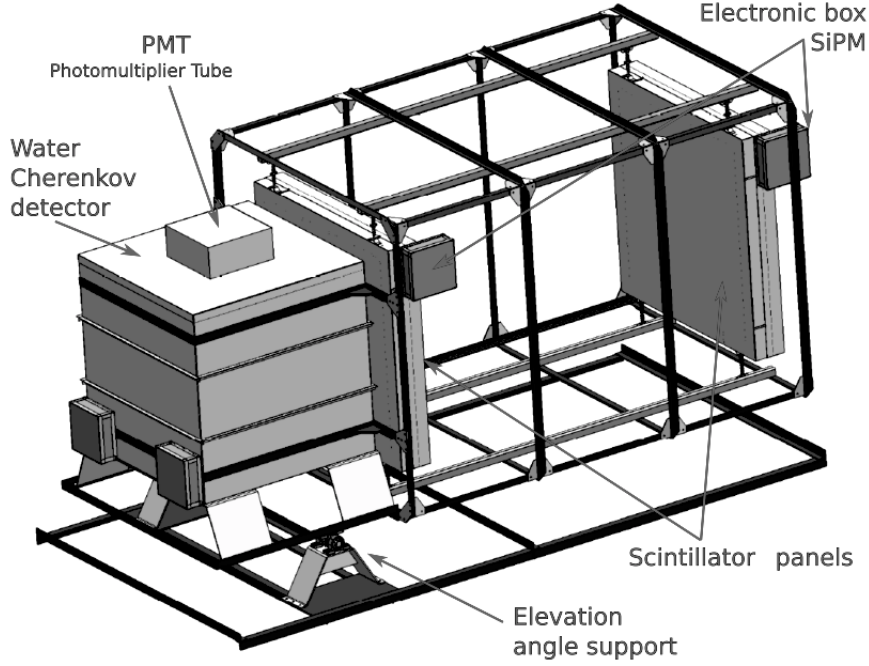


Figure 1. A sketch of the hybrid detector *MuTe*: a two-panel scintillator bar hodoscope in front and a Water Cherenkov Detector (WCD) at the back. Each panel of the scintillator bar hodoscope has 900 detection pixels to determine the incoming directions of the particles. The *WCD* is a stainless steel container of 120cm side, coated inside with Tyvek, holding a *PMT* at the center of the roof to detect the Cherenkov radiation and devised to filter most of the backward & background noise of muography. The mechanical structure has a variable elevation angle to adjust the telescope according to the object under study, and it is possible to adjust scintillator panels separation to modify the pixel spatial resolution.

hodoscope panels to the passage of charged particles, especially in the Minimum Ionization Particle (*MIP*) energy range.

3.1 The scintillator bar model

The *Geant4* geometric model of the bar consist of a parallelepiped 4cm high, 1cm wide and 120cm long. We incorporate to this geometry a coating material –15% TiO_2 and 85% polystyrene– with a reflectivity of 1 and 0.25mm thickness.

The polystyrene scintillation bar has an index of refraction= 1.50, and a photon absorption length of 5.5cm. There is a tunnel 119.5cm long and 1.8mm diameter, drilled through the central axis of the bar, where a multi-cladded *WLS* fiber is placed. The 0.5cm stop at the end of the tunnel –filled with air to make the model as real as possible– prevents the escape of photons. The fiber length (119.45cm) allows the *SiPM* to be located inside the tunnel.

A solid cylinder of poly-methyl methacrylate, 119.45cm long and 0.5mm radius, models the fiber. The first cladding of this fiber is a cylindrical shell of polyethylene, with an internal radius of 0.5mm and an external radius of 0.515mm. The second is a shell of fluorinated polyethylene, with an internal radius of 0.515mm and an external radius of 0.530mm. Both coatings have the same fiber length.

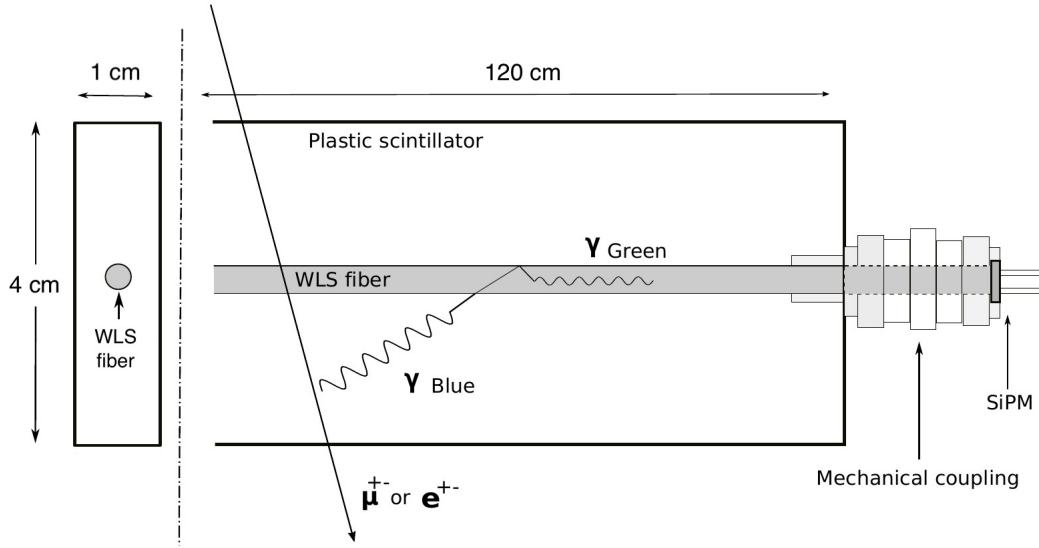


Figure 2. This sketch represents the scintillator bar system, with an embedded *WLS* fiber placed in the center of the plastic scintillation bar and coupled to a *SiPM*. Charged particles crossing the bar produce scintillation photons in the blue-violet band. Those photons are absorbed and re-emitted in the *WLS* fiber as green photons. The fiber guides photons to the *SiPM* where they can produce a signal depending on their wavelength, as the *SiPM* spectral detection range is from 270 to 900 nm, with the maximum sensitivity around 450 nm.

A square surface of side 1.3mm attached to one end of the fiber, represents the *SiPMs*. The simulation allow to set the *SiPM* photon detection efficiency, which depends on the wavelength of the photon hitting the *SiPM*, where the highest probability of Photo-Electrons (*pe*) generation is around 470nm [38].

Figure 3 displays the simulation results of the scintillator bar response to charged particles of different energies. The histogram of the number of photo-electrons generated by 10000 electrons of 20MeV, 100MeV and 500MeV has the same profile as those corresponding to the 10000 muons of 1GeV, 10GeV and 100GeV. This similarity occurs because both these particles have the same stopping power in polystyrene, i.e. $\frac{dE}{d\epsilon_{\text{pol}}} \approx 2 \text{ MeV cm}^2/\text{g}$ [41], so they all deposit about 2.08MeV of energy when passing through a centimeter of polystyrene. Therefore our detector is not able to distinguish muons from electrons, and it is necessary to use the *WCD* to select the muon events from noise.

The mean value of these histograms is around 40*pe*, which is equivalent to 2.08MeV of energy deposited in the bar since those particles pass through vertically and the distance traveled is 1 cm. The following simulations are for muons with 3GeV, which are the most frequent at the level of our observation point on the Cerro Machín volcano, thus, from now on, the *MIP* refers to this particular particle having this energy.

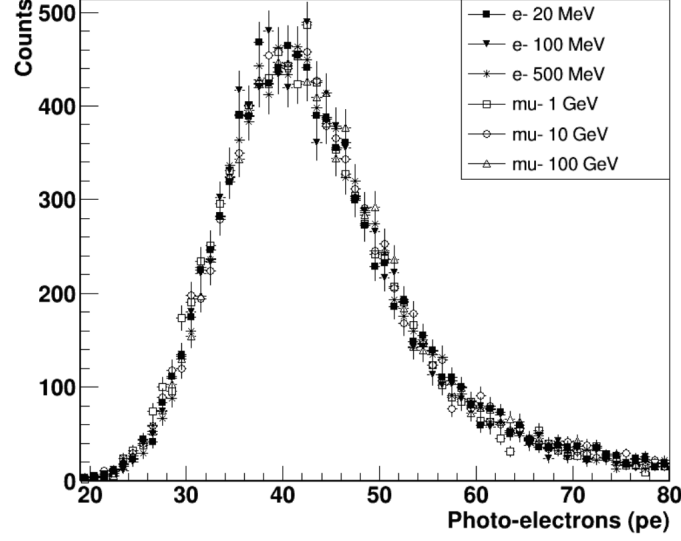


Figure 3. Scintillator bar response to *MIPs* of different energy. As expected, both electrons and muons generate the same histogram profile, since the energy loss of all those particles is $\sim 2.08\text{MeV}$. This result validates the code used and therefore supports the veracity of the simulations of the scintillator bar. To obtain those histograms, we performed the interaction of 10000 particles (of each energy and type) with the bar. The average number of photo-electrons is around $40pe$ for all the particles, i.e., this detector is not able to distinguish muon events from noise.

3.1.1 Attenuation of the photons in the *Bar-Fiber-SiPM* system

The light that propagates within the *WLS* fiber suffers an inevitable attenuation due to some photons escape from the optical guide, and others can be absorbed by the material while being transported to the *SiPM*. This attenuation depends on the path traversed by the photons, and so on the distance between the impinging particle and the *SiPM*.

From the simulations of the scintillation detector, we can count the number of *pe* generated in the *SiPM* when a *MIP* crosses the bar at different distances x , where x is the distance between the point of impact and the location of the *SiPM*. These distances were chosen so as to take into account the width of the pixels of the hodoscope, i.e., 4cm wide; therefore x varies as, $x = (2 + 4p)\text{cm}$ $p = 0, 1, 2, \dots, 29$.

Figure 4 shows the result of this simulation. If the particle impacts at the position closest to the *SiPM* (i.e. $x = 2\text{cm}$), it has the maximum photo-electron intensity and, if it impacts farther away from the *SiPM*, the intensity decreases. A double exponential function $F(x)$ fits the data and models this decrease

$$F(x) = 0.468e^{-0.003(2-x)} + 0.531e^{0.005(2-x)}. \quad (3.1)$$

From this plot, we have that the attenuation in the *Bar-Fiber-SiPM* system is around 7%, that agrees with the experimental results, $\sim 11\%$ [42], and show in figure 10.

The *MIP* detection with scintillator bar generates a number of *pe* in the *SiPM* at a time t . Now we want to estimate the time needed to collect the total number of photo-electrons produced. This total is about $40pe$ at $x = 2\text{cm}$, while at $x = 118\text{cm}$ it is about $37pe$. From the left of figure 5 it can be seen that 40% of the total photo-electrons occurred in the first 10ns when the *MIP* has impacting

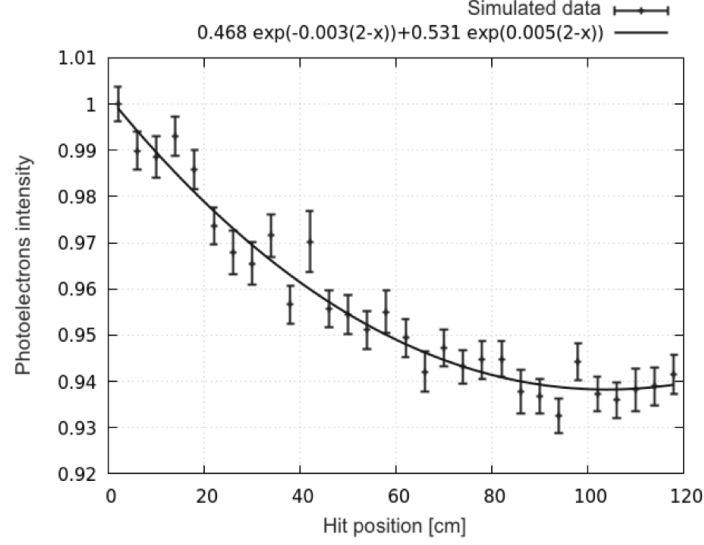


Figure 4. The number of photo-electrons versus the position of the impacting *MIP* in the bar. At $x = 2\text{cm}$, we have the maximum photo-electron intensity, and as the particle impacts farther away to the *SiPM*, the intensity decreases. A double exponential function fits the simulated data, and this behavior can be associated with the attenuation of the photons traveling through the fiber being about 7%

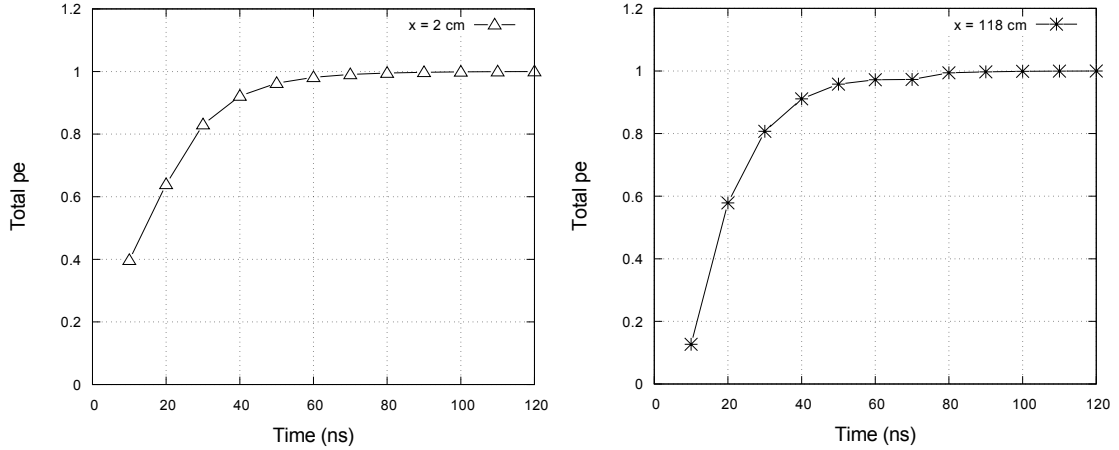


Figure 5. Cumulative number of photo-electrons produced when a *MIP* hits the bar at 2cm from the *SiPM* (left) and at 118cm (right). It can be noticed that 40% of the Total *pe* occurred in the first 10ns when $x = 2\text{cm}$ and when $x = 118\text{cm}$, only 12% of the *pe* occurred in the same time. In both cases, the total number of *pe* is reached in about 80ns, that is, the average time necessary to collect the total of *pe* produced by the passage of a muon, at any point of impact in the bar.

the bar at 2cm from the *SiPM*. Observe from the right of figure 5 –when the *MIP* has impacted 118cm from the *SiPM*–, that only 12% of the *pe* is produced in the same time. In both cases, the total number of *pe* is reached around 80ns, that is, the average time necessary to collect the total of *pe* produced by the passage of a muon, at any point of impact in the bar.

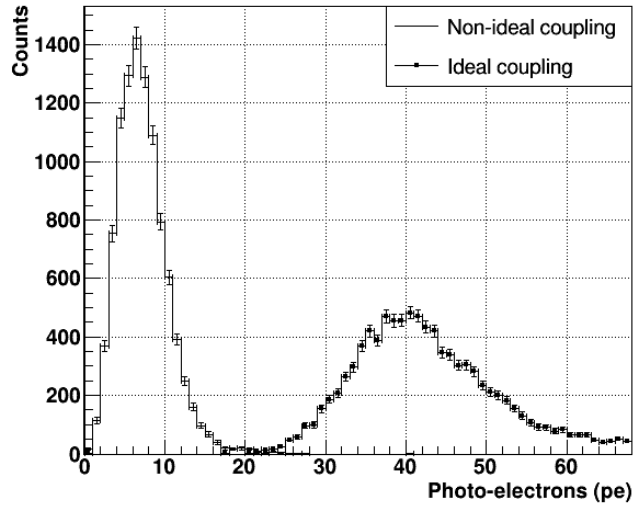


Figure 6. Histogram of the number of pe resulting from the evaluation of the $SiPM$ and fiber coupling. The squares curve represents the photo-electrons produced in the ideal case (when the $SiPM$ and the fiber are side by side), while the simple line shows the non-ideal case, where the distance between the $SiPM$ and the fiber is 1.15mm. The average number in the ideal case is around $40pe$ and in the non-ideal is around $8pe$, i.e. the 80% of the signal is lost. This result gives an idea of when a bar-fiber- $SiPM$ system of the real detector is badly coupled and should be replaced or verified.

3.1.2 SiPM and fiber coupling

The *Geant4* model allows estimating how good is the coupling between the $SiPM$ and the fiber. We define the ideal $SiPM$ -fiber when they are optically coupled, without any space between them. Thus, all the traveling photons at the edge of the fiber impact directly on the $SiPM$. As shown above, the obtained average number of photo-electrons, for an ideal coupling, is $40pe$. The non-ideal coupling had an airspace (filled with air) of 1.15mm in between the $SiPM$ and the fiber. The number of pe is reduced to 8, representing a loss of 80% of the signal compared to the ideal case, as shown in figure 6.

3.2 Experimental results from the scintillator detector

As described before, the plastic scintillators of the *MuTe* panels allow the indirect detection of ionizing radiation from the analysis of the electrical signal produced in the $SiPMs$. Since the $SiPMs$ have noise, it is essential to calibrate the so as to correctly interpret the measured data. To start with, the $SiPM$ must work in the Geiger mode at any temperature. In section 3.2.1 presents the dependence between the breakdown voltage and temperature is presented.

Due to the fact that the scintillator bar (120cm long) has an average attenuation length of 5.5cm for photons, we are forced to use a WLS fiber to guide them from the point they were created to the $SiPM$. Thus we must calibrate for the attenuation in the WLS fiber due to the length travelled by the photons (see section 3.2.2).

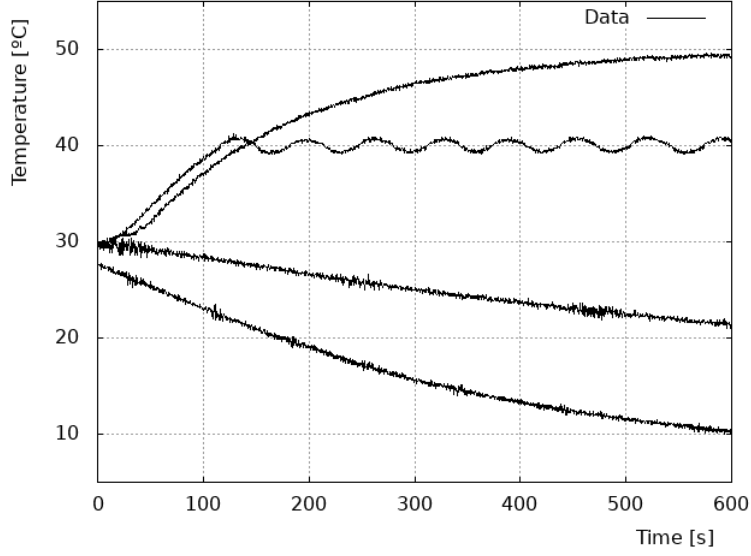


Figure 7. Measurements of the system set-up time with different target temperatures: 10°C, 20°C, 40°C and 50°C. We can see that the time required to reach the target temperature in each case is around (600 ± 50) s.

3.2.1 Dependence of the breakdown voltage with temperature

To study the response of each scintillator bar, we first studied the *SiPMs* thermal stability. As mentioned above, we want the *SiPMs* to operate in the Geiger mode. *SiPMs* can change their mode of operation if the input voltage (V_{Bias}) is less than the breakdown voltage (V_B), and this parameter varies with temperature. Thus we need to find this functionality to guarantee that *SiPMs* always works in Geiger mode.

To establish this dependence, we built a temperature-controlled box regulated by a TEC1-12706 thermoelectric Peltier cell, mounted on an aluminum frame, where we placed the *SiPM*. The control system consists of two sensors: one that controls the temperature and the other to measure it on the *SiPM*. Figure 7 shows the results for different target temperatures (10°C, 20°C, 40°C and 50°C). Note that the time required to reach the target temperature, in each case, is around (600 ± 50) s.

Next, Dark-Current [43] measurements ranging from 0 to 50°C illustrate (see figure 8) the linear dependence of V_B with temperature. It is clear that for each 10°C of temperature, the V_B changes around 0.45V.

3.2.2 Attenuation measurements of the Bar-Fiber-SiPM system

To estimate the attenuation in the bar-fiber system, we measure the signal produced by the passage of charged particles at both ends and the middle of the bar. Figure 9 illustrates the experimental set-up, in which a particle is detected only if there is a simultaneous signal in all the three scintillators: the upper, the bar, and the lower one.

The trigger system, connected to a RedPitaya development card, records pulses with a frequency of 125 MHz [44]. The system was synchronized for coincidence pulses, providing three input signals to the card and one output signal that corresponds to each position in the scintillator test bar. The coincidence system has an angle θ for this configuration of 106.26°, as shown in Figure 9. The

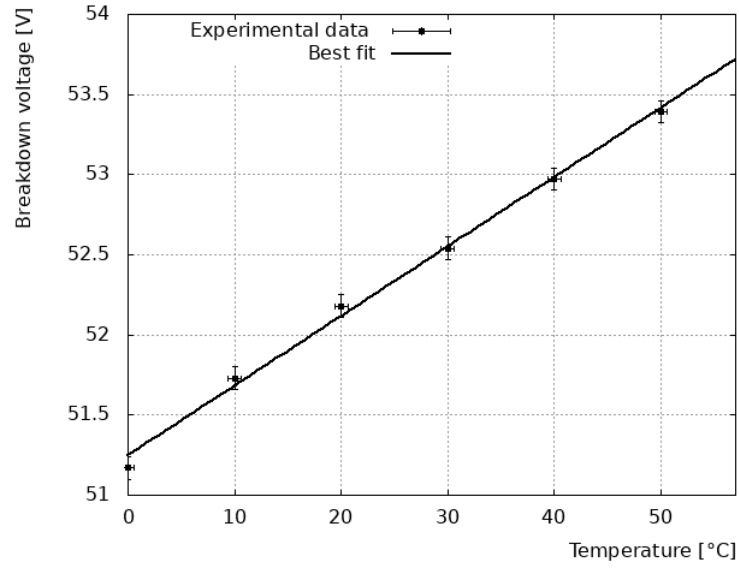


Figure 8. Dependence of the breakdown voltage with the temperature for the *SiPM* Hamamatsu S13360-1350CS used in the MuTe hodoscope. It can be observed that the relation is linear, that is for every 10°C of temperature the V_B varies about 0.45V.

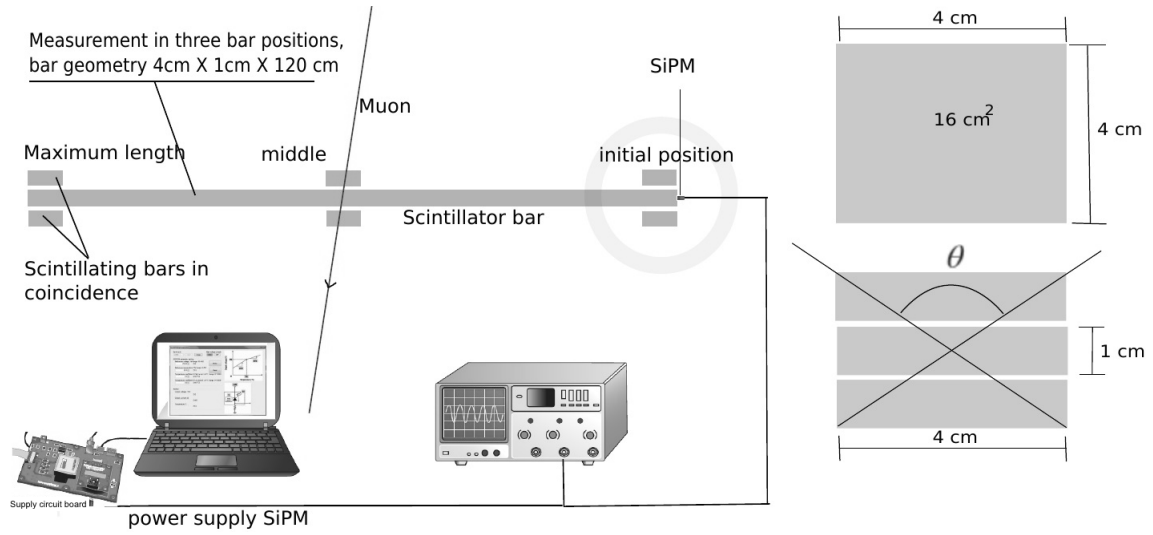


Figure 9. Diagram of the experimental set-up to measure the bar-fiber signal attenuation. The three positions of interest are at both ends and the middle. An event is genuine if there is a simultaneous signal in the three scintillators: the upper, the bar, and the lower one.

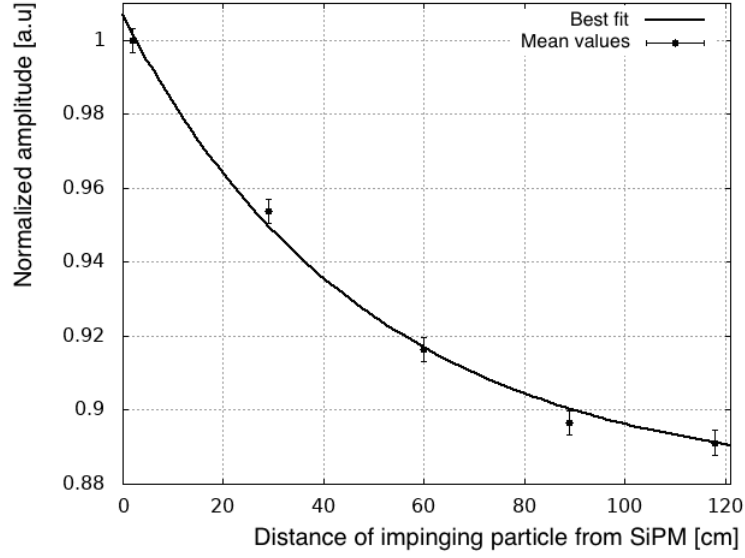


Figure 10. Attenuation of the signal in the test bar obtained from the coincidence of three signals. The maximum amplitude is in the position closest to the *SiPM*, decreases by 11% at the opposite end.

frequency of events per minute, measured with an oscilloscope, was 10 ± 1 per minute for 16cm^2 . Thus, with this rate, it is possible to detect $0.62 \text{ particles} \times \text{min} \times \text{cm}^2$.

After a noise calibration, we record 10000 pulses in the three positions. At the farthest end from the *SiPM*, the fiber was cut at 45° to maximize photon leakage and to avoid secondary pulses due to reflections at the end of the fiber.

From each averaged pulse, we calculated the mean charge deposited at the three positions. Then, we estimated the percentage of attenuation by normalizing and comparing the values, as shown in Figure 10. In our case, the difference between the mean charge value deposited at both ends is around 11%. The following exponential function fits the attenuated signal.

$$H(x) = 0.880 + 0.126e^{(-0.02x)}. \quad (3.2)$$

3.3 Simulated attenuation in the hodoscope

The probability of producing photo-electrons in the horizontal and vertical scintillators bar is a crucial concept in determine the response of each panel of the hodoscope. The bar simulation generates the response of a detection panel to *MIPs*. Thus, independent events in a particular pixel $P_{i,j}^F$ is given by

$$P_{i,j}^F = P_i^F \times P_j^F, \quad (3.3)$$

where P_i^F y P_j^F are the probabilities obtained in the horizontal bar i and in the vertical bar j , respectively.

Figure 11 displays the probability of photo-electrons produced by 3 GeV muons striking each panel pixel, obtained from equation 3.3.

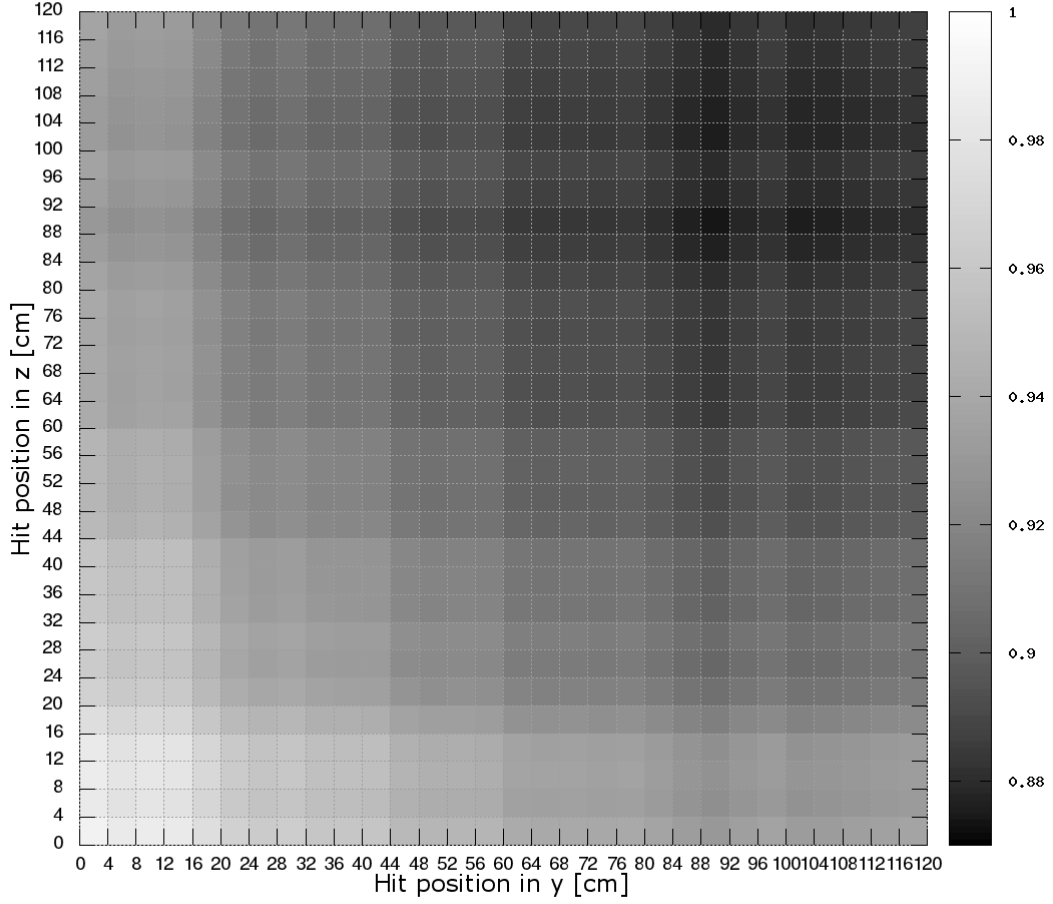


Figure 11. The probability of photo-electron production in each pixel of a hodoscope panel by muons of 3 GeV of energy. Each frame represents a detection pixel and it can be seen that there is a difference between two zones of the panel. In pixel P_{11} , where the incoming muon is closest to the *SiPMs*, the maximum number of *pe* are produced; the number decreasing with distance up to a 12% at the furthest position. This result is valid both for the front and the rear panel.

These results are valid for both the front panel and the rear panel, and from figure 11, it clear that there is a difference between the zones. This difference around 12% can be associated with the attenuation of photons in the fiber, i.e., the pixels that are closer to the *SiPM* count more photo-electrons.

4 The water Cherenkov detector response to cosmic background radiation

The *WCD* indirectly detects charged secondaries, by the Cherenkov photons generated by relativistic particles traveling through the water. The photo-multiplier tube detects photo-electrons according

to its quantum efficiency, which depends on the wavelength of the impacting photon. In our case, the *PMT* Hamamatsu R5912 in the *WCD* has a maximum detection probability value of 25% for photons with $\lambda = 400$ nm [38]. The *PMT* is located at the top of the metal tank (with 120 cm sides) which is coated with a diffusive lining of Tyvek and filled with purified water. Next we will discuss some results from the detector simulation, as well as the first data recorded by the *WCD*. In *Geant4* the water container is a stainless steel cube of length $l_c = 1.21$ m, with the water inside as a cube of sides $l = 1.20$ m. The water has a refractive index n , which varies between 1.3435 and 1.3608, and a photon absorption length ranging from 0.69 m to 2.90 m depending on its energy. In the inside walls of the cube, the Tyvek is modeled as an optical surface with a reflection index $n_{\text{Tyvek}} = 1$, which diffuses the Cherenkov photons.

For the *PMT*, the photo-cathode was simulated as a half-ellipsoid of air with semiaxes $s_x = 10.1$ cm, $s_y = 10.1$ cm and $s_z = 6.5$ cm, located on top of the water cube. The Quantum Efficiency (*QE*) of this device was introduced in the code, taking into account the reference data of the Hamamatsu R5912 [38]. The *QE* determines whether photons reaching the outer surface of the photo-cathode will be detected or not. These photons originate photo-electrons (denoted as *pe*) by photoelectric effect. The *WCD* response is given in terms of *pe* generated by each particle interacting with it.

Notice that the inclusion of the *QE* of the *PMT* in the code, as a function dependent on λ , represents an improvement over the simulations of *WCDs* carried out previously in our research group. An efficiency of 25% was used, as in [45], for the wavelength range between 330 nm and 570 nm. Therefore, the new code offers more precise results of the pulses produced by the passage of particles through the water.

4.1 Estimation of the Vertical Equivalent Muon unit

The Vertical Equivalent Muon (*VEM*) –defined as the average charge collected in the *PMT* when a high-energy muon vertically crosses the entire detector – is generally adopted as the unit in the calibration of the energy deposited by incident particles and is independent of the detection position. Muons can be easily identified by installing plastic scintillators above and below the *WCD* [46].

The *Geant4* code allows the injection of muons with a chosen energy and direction. In the model we model inject 100000 vertical muons with 3 GeV in direction $-\hat{z}$ towards the water, and the initial position given by the point $P = (80, 80, 121)$ cm, over the *WCD*. The portion of the number of Cherenkov photons, N , that reaches the external surface of the photo-cathode, is N_{PMT} .

The N_{PMT} , depending on its wavelength, produces a number of photo-electrons, N_{pe} . We have estimated the efficiency of the *WCD* in the following way: one *VEM* of 3 GeV generates around 46857 Cherenkov photons in 120 cm. Next, only 1617 of those photons reach the external surface of the photo-cathode, and, due to its quantum efficiency, around an average 203.2 *pe* were produced. Thus, the system has a muon detection efficiency of 0.4%, that is,

$$\eta_{\text{WCD}} = \frac{N_{\text{FE}}}{N} 100\% = \frac{203.2}{46857} 100\% = 0.4\% \quad (4.1)$$

Figure 12 compares the simulated value of the *VEM* (~ 203.2 pe) with the measured (~ 167.5 pe). This figure represents the *pe* histogram for one hour of data collection at a discrimination threshold of 110 mV. The histogram has two prominent humps, the electromagnetic (electrons, positrons and gammas) hump at ~ 70 pe and the muonic hump at ~ 167.5 pe [18].

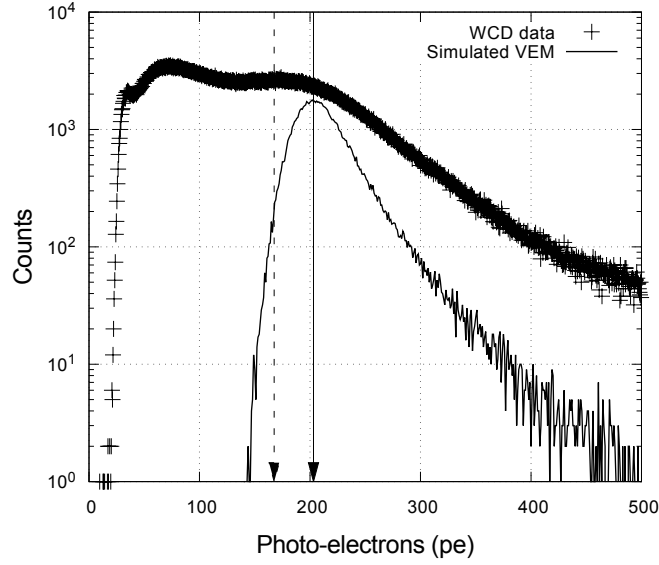


Figure 12. Photo-electron histogram for one hour of data recorded by the *WCD* with a discrimination threshold of 110mV. The histogram has two prominent humps, the electromagnetic at $\sim 70pe$ and the muonic hump at $\sim 167.5pe$. The solid curve represents the simulated *VEM* histogram whose mean value is $\sim 203.2pe$ (solid arrow), for comparison with the measured value (dashed arrow).

Table 1. Summary of the physical magnitudes obtained for the *VEM* and the *VE*: Length traveled in water (l), Number of Cherenkov Photons produced (N), Number of Photons that reach the *PMT* (N_{PMT}), Number of Photoelectrons (N_{pe}), Time of attenuation of the pulse (τ) and Length of attenuation (l_a).

	$\mu^- (3 \text{ GeV})$	$e^- (20 \text{ MeV})$
l	$(120 \pm 1) \text{ cm}$	$(10 \pm 1) \text{ cm}$
N	46857 ± 13	3538 ± 1
N_{PMT}	1617 ± 1	132.1 ± 0.1
N_{pe}	203.2 ± 0.2	16.729 ± 0.003
τ	$(42.12 \pm 0.01) \text{ ns}$	$(32.75 \pm 0.03) \text{ ns}$
l_a	$(7.332 \pm 0.001) \text{ m}$	$(9.430 \pm 0.002) \text{ m}$

To compare the *WCD* response to muons and electrons at the Cerro Machín Volcano, we run simulations for 100000 vertical electrons, *VE*, of 20MeV at the same initial direction and point *P*. Figure 13 presents the corresponding histogram of the number of photo-electrons. The mean value of the *VE* is smaller than the *VEM*, $\sim 16.7pe$ due to the *VE* is smaller by $\sim 8\%$ than for the *VEM*.

Next, in figure 14 are shown the number of pe versus time for both *VEM* (top) and *VE* (bottom) pulses. From the best fits to the histograms, we obtain both attenuation: time and length. Finally, the table 4.1 summarize the comparison between both charged particles.

4.2 *WCD* response to the cosmic ray background radiation

The *LAGO ARTI* framework allows to estimate the response of the *WCD* to the cosmic ray background radiation flux (Ξ) at any site [47]. This toolkit employs a *Geant4* code to estimate the number of Cherenkov photons detected by the *PMT* with its quantum efficiency. The *ARTI* frame-

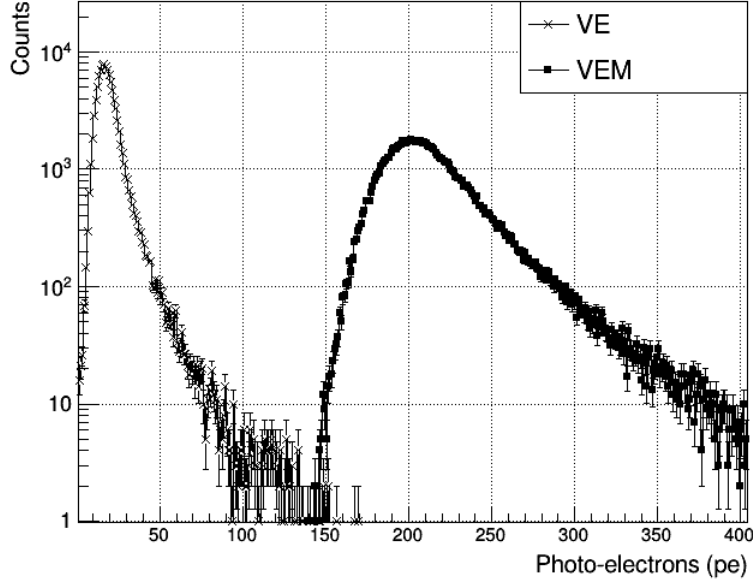


Figure 13. Histogram of the number of photo-electrons produced due to the detection of vertical muons (squares) and vertical electrons (crosses) with the *WCD*. From the *VEM* curve its mean is $\pm 203.2pe$ compared to $16.7pe$ for *VE*, that is the 8% of the *VEM*.

work uses the energy and the momentum of the particles from Ξ as input and obtains the flux by using the *CORSIKA* code [48], with a geomagnetic correction from the *MAGCOS* code [49]. For other examples of the precise simulation chain see [50, 51].

Figure 15 plots the histogram of the number of photo-electrons produced, by all particles, at Cerro Machín. The flux Ξ_{CM} ,

$$\Xi_{CM} = \frac{N_{Sec}}{7.5 \text{ s } 480 \text{ m}^2}, \quad (4.2)$$

is calculated over a circular area $A = 480 \text{ m}^2$ placed 1cm above the detector, with a zenith aperture of $0 \leq \theta \leq 80^\circ$, and where N_{Sec} represents the number of secondaries at this particular site.

The different curves represent the contribution of various particles to the total response (empty circles). Note that this curve has two main peaks, the first one due to the contribution of the electromagnetic component and the second one due to the muonic component.

5 Conclusions

As we have stated above, our MuTe combines two detection techniques: a hodoscope with two detection panels of plastic scintillator bars, and a *WCD*, in an innovative setup which differentiates it from some previous detectors.

- **Scintillators panels:** Inspired by the experiences of other volcano muography experiments [52, 53], we have designed two X-Y arrays of 30×30 plastic scintillating strips ($120\text{cm} \times 4\text{cm} \times 1\text{cm}$), made with StyronTM 665-W polystyrene doped with a mixture of liquid

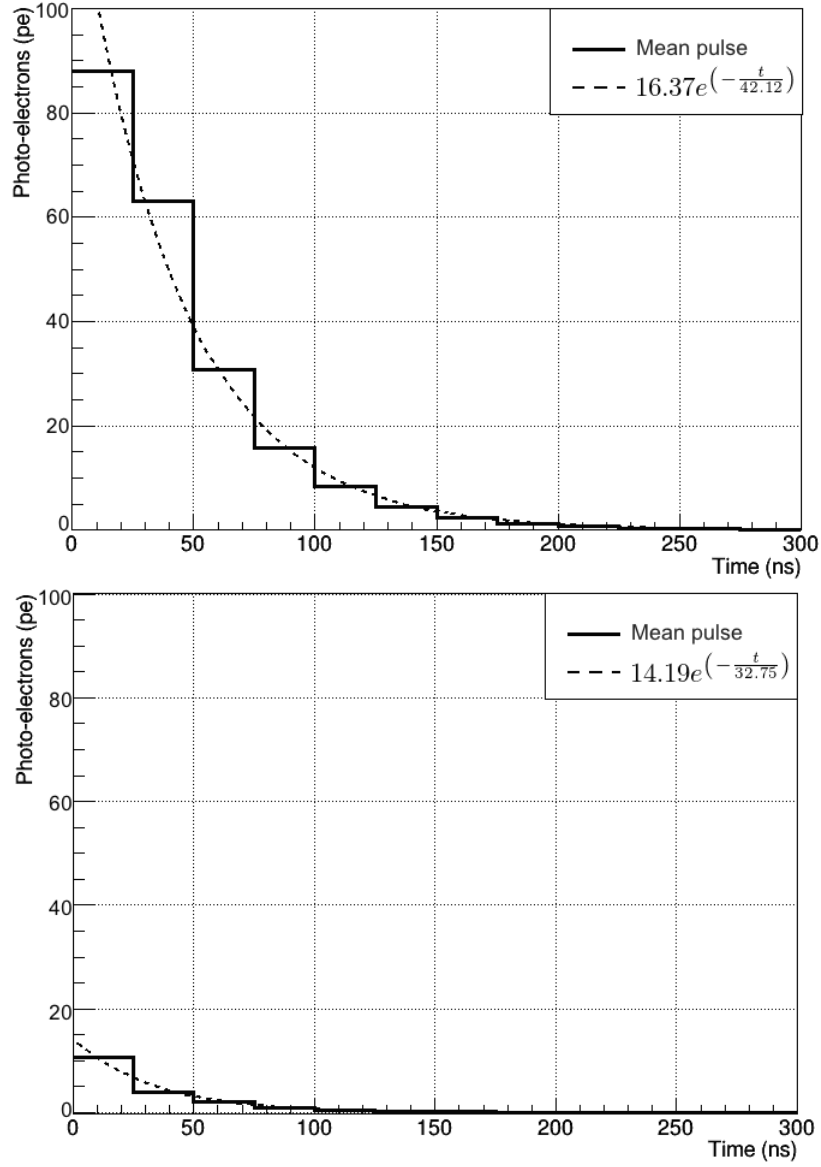


Figure 14. Mean pulse corresponding to the *VEM* (top) and the *VE* (bottom) response. The dashed lines represent the best exponential fit of the pulses where the attenuation time τ is around 42.12ns for the *VEM* and 32.75ns for the *VE*.

organic scintillators: 1% of 2,5-diphenyloxazole (PPO) and 0.03% of 1,4-bis (5-phenyloxazol-2-yl) benzene (POPOP). Each array has 900 pixels of $4\text{ cm} \times 4\text{ cm} = 16\text{ cm}^2$, which sums up $14,400\text{ cm}^2$ of detection surface which can be separated up to a distance of 250 cm.

- **Water Cherenkov Detector:** The *WCD* is a purified water cube of 120 cm side, located behind the rear scintillator panel, which acts as an absorbing element and as a third active coincidence detector. Due to its dimensions and location, it filters most of the background noise (low energies electrons, protons, and muons moving backward), which could cause overestimation in the hodoscope counts [34], and is capable of isolating the muonic component

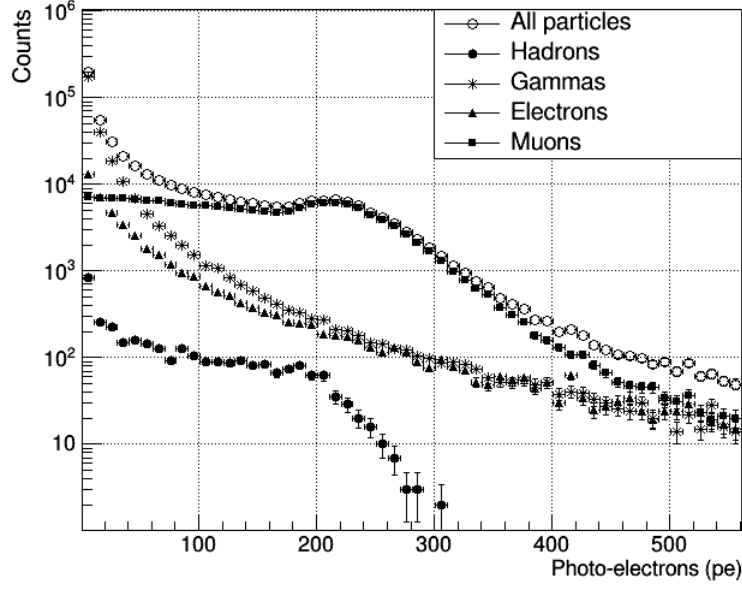


Figure 15. Histogram of the number of photo-electrons produced by all particles detected in the *WCD*. The histogram has two prominent humps at $\sim 5pe$ and at $\sim 210pe$. It should be noted that the first one is dominated by the electromagnetic component while the second by the muonic component.

of the incident particle flux. From the charge histogram, obtained by time integration of the individual pulses measured in the *WCD*, it is possible to separate two components of the incident flux: electromagnetic part (photon, electron & positron) and the μ -component [50].

The Colombian *MuTe* combines particle identification techniques to discriminate noise background from data. It filters the primary noise sources for muography, i.e., the soft-component (e^\pm) of *EAS* and scattered/upward-coming muons. Particle deposited energy identifies Electrons/positrons events in the *WCD*, while rejects scattered and backward muons using a pico-second Time-of-Flight system.

From the *Geant4* modeling of the scintillator detector, we obtain that the number of pe decreases about 7%, with respect to those produced at the near end of the *SiPM*. This reduction occurs due to the attenuation of the photons that travel in the fiber, since, the more distance they travel within it, the more energy they lose and less photons reach the *SiPMs*. This result is in agreement with the 11% attenuation obtained with the experimental setup described in section 3.2. This attenuation seems to be insignificant in the bar, but it is more noticeable in the hodoscope panels, since, the difference between the closest corner to the *SiPMs* and the furthest, is around 12%.

Regarding the *WCD* response, the value of simulated *VEM* and those recorded in the laboratory measurements, are of the same order of magnitude but present a percentage difference of 18% with respect the simulated value. This difference can be assigned to the various electronic components, where part of the signal is lost.

From the results obtained, a muon detection trigger for the *MuTe* is proposed in terms of the energy deposited in each of its components. That is, the muon must deposit about $2.08MeV$ in two

scintillator bars on the front panel, then about the same energy in two bars on the rear panel of the hodoscope, and finally be discriminated from the noise in the *WCD*. Lastly the muon must lose about 240MeV of energy to be counted as an event.

Acknowledgments

The authors acknowledge the financial support of Departamento Administrativo de Ciencia, Tecnología e Innovación de Colombia (ColCiencias) under contract FP44842-082-2015 and to the Programa de Cooperación Nivel II (PCB-II) MINCYT-CONICET-COLCIENCIAS 2015, under project CO/15/02. We are also very thankful to LAGO and to the Pierre Auger Collaboration for their continuous support. The simulations in this work were partially possible thanks to The Red Iberoamericana de Computación de Altas Prestaciones (RICAP, 517RT0529), co-funded by the Programa Iberoamericano de Ciencia y Tecnología para el Desarrollo (CYTED) under its Thematic Networks Call. We also thank the computational support from the Universidad Industrial de Santander (SC3UIS) High Performance and Scientific Computing Centre. We would also like to thank Vicerrectoría Investigación y Extensión Universidad Industrial de Santander for its permanent sponsorship. We acknowledge very fruitful discussions with D. Sierra-Porta.

References

- [1] J. Marteau, D. Gibert, N. Lesparre, F. Nicollin, P. Noli, and F. Giacoppo. Muons tomography applied to geosciences and volcanology. *Nuclear Instruments and Methods in Physics Research Section A: Accelerators, Spectrometers, Detectors and Associated Equipment*, 695:23 – 28, 2012. New Developments in Photodetection NDIP11.
- [2] R. Kaiser. Muography: overview and future directions. *Philosophical Transactions of the Royal Society A: Mathematical, Physical and Engineering Sciences*, 377(2137):20180049, January 2019.
- [3] G. Blanpied, S. Kumar, D. Dorroh, C. Morgan, I. Blanpied, M. Sossong, S. McKenney, and B. Nelson. Material discrimination using scattering and stopping of cosmic ray muons and electrons: Differentiating heavier from lighter metals as well as low-atomic weight materials. *Nuclear Instruments and Methods in Physics Research Section A: Accelerators, Spectrometers, Detectors and Associated Equipment*, 784:352–358, jun 2015.
- [4] K. Morishima, M. Kuno, A. Nishio, N. Kitagawa, Y. Manabe, M. Moto, F. Takasaki, H. Fujii, K. Satoh, and H. Kodama. Discovery of a big void in khufu’s pyramid by observation of cosmic-ray muons. *Nature*, 552(7685):386, 2017.
- [5] H. Gómez, C. Carloganu, D. Gibert, J. Jacquemier, Y. Karyotakis, J. Marteau, V. Niess, S. Katsanevas, and A. Tonazzo. Studies on muon tomography for archaeological internal structures scanning. In *Journal of Physics: Conference Series*, page 052016. IOP Publishing, 2016.
- [6] H. Fujii, K. Hara, S. Hashimoto, F. Ito, H. Kakuno, S.H. Kim, M. Kochiyama, K. Nagamine, A. Suzuki, Y. Takada, Y. Takahashi, F. Takasaki, and S. Yamashita. Performance of a remotely located muon radiography system to identify the inner structure of a nuclear plant. *Progress of Theoretical and Experimental Physics*, 2013(7), jul 2013.
- [7] G. Saracino, L. Amato, F. Ambrosino, G. Antonucci, L. Bonechi, L. Cimmino, L. Consiglio, R. D.’Alessandro, E. De Luzio, G. Minin, P. Noli, L. Scognamiglio, P. Strolin, and A. Varriale. Imaging of

underground cavities with cosmic-ray muons from observations at mt. echia (naples). *Scientific Reports*, 7(1), apr 2017.

- [8] L. F. Thompson, J. P. Stowell, S. J. Fargher, C. A. Steer, K. L. Loughney, E. M. O’Sullivan, J. G. Gluyas, S. W. Blaney, and R. J. Pidcock. The application of muon tomography to the imaging of railway tunnels. *arXiv e-prints*, page arXiv:1906.05814, Jun 2019.
- [9] H. K. M. Tanaka and L. Oláh. Overview of muographers. *Philosophical Transactions of the Royal Society A: Mathematical, Physical and Engineering Sciences*, 377(2137):20180143, January 2019.
- [10] G.P. Cortés. Informe de actividad volcánica segmento norte de colombia diciembre de 2016. Technical report, Reporte interno, Manizales, Colombia. INGEOMINAS, 2016.
- [11] A. Agudelo. Informe técnico de actividad de los volcanes nevado del huila, puracé y sotará, durante el periodo de diciembre de 2016. Technical report, Reporte Interno, Popayan, Colombia, Servicio Geológico Colombiano, 12 2016.
- [12] E. Muñoz. Informe mensual de actividad de los volcanes galeras,cumbal,chiles y cerro negro, las ánimas, dona juana y azufral. Technical report, Reporte interno, Pasto, Colombia. INGEOMINAS, 2017.
- [13] H. Asorey, L. A. Núñez, J. D. Sanabria-Gómez, C. Sarmiento-Cano, D. Sierra-Porta, M. Suarez-Duran, M. Valencia-Otero, and A. Vesga-Ramírez. Muon Tomography sites for Colombia volcanoes. *ArXiv e-prints*, May 2017.
- [14] H. Asorey, R. Calderón-Ardila, C. R. Carvajal-Bohorquez, S. Hernández-Barajas, L. Martínez-Ramírez, A. Jaimes-Motta, F. León-Carreño, J. Peña-Rodríguez, J. Pisco-Guavabe, J.D. Sanabria-Gómez, M. Suárez-Durán, A. Vásquez-Ramírez, K. Forero-Gutiérrez, J. Salamanca-Coy, L. A. Núñez, and D. Sierra-Porta. Astroparticle projects at the eastern colombia region: facilities and instrumentation. *Scientia et technica*, 23(3):391–396, 2018.
- [15] H. Asorey, R. Calderón-Ardila, K. Forero-Gutiérrez, L. A. Núñez, J. Peña-Rodríguez, J. Salamanca-Coy, J.D. Sanabria-Gómez, J. Sánchez-Villafrades, and D. Sierra-Porta. minimate: A muon telescope prototype for studying volcanic structures with cosmic ray flux. *Scientia et technica*, 23(3):386–390, 2018.
- [16] I.D. Guerrero, D.F. Cabrera, J.C. Paz, J.D. Estrada, C.A. Villota, E.A. Velasco, F.E. Fajardo, O. Rodriguez, J. Rodriguez, D. Arturo, D. Dueñas, D. Torres, J. Ramirez, J. Revelo, G. Ortega, D. Benavides, J. Betancourt, A. Tapia, and D.A. Martínez-Caicedo. Design and construction of a muon detector prototype for study the galeras volcano internal structure. In *Journal of Physics: Conference Series*, page 012020. IOP Publishing, 2019.
- [17] J.S. Useche-Parra and C.A. Avila-Bernal. Estimation of cosmic-muon flux attenuation by monserrate hill in bogota. *Journal of Instrumentation*, 14(02):P02015, 2019.
- [18] J. Peña-Rodríguez, A. Vásquez-Ramírez, J. Sanabria-Gómez, L. Núñez, D. Sierra-Porta, and H. Asorey. Calibration and first measurements of mute: a hybrid muon telescope for geological structures. In *36th International Cosmic Ray Conference (ICRC2019)*, volume 36, 2019.
- [19] A. Anastasio, F. Ambrosino, D. Basta, L. Bonechi, M. Brianzi, A. Bross, S. Callier, A. Caputo, R. Ciaranfi, L. Cimmino, R. D’Alessandro, L. D’Auria, C. de La Taille, S. Energico, F. Garufi, F. Giudicepietro, A. Lauria, G. Macedonio, M. Martini, V. Masone, C. Mattone, M.C. Montesi, P. Noli, M. Orazi, G. Passeggio, R. Peluso, A. Pla-Dalmau, L. Raux, P. Rubinov, G. Saracino, E. Scarlini, G. Scarpato, G. Sekhniaidze, O. Starodubtsev, P. Strolin, A. Taketa, H.K.M. Tanaka, and A. Vanzanella. The mu-ray detector for muon radiography of volcanoes. *Nuclear Instruments and*

Methods in Physics Research Section A: Accelerators, Spectrometers, Detectors and Associated Equipment, 732:423 – 426, 2013. Vienna Conference on Instrumentation 2013.

- [20] C. Carloganu, V. Niess, S. Bene, E. Busato, P. Dupieux, F. Fehr, P. Gay, D. Miallier, B. Vulpescu, and P. Boivin. Towards a muon radiography of the puy de dôme. *Geoscientific Instrumentation, Methods and Data Systems*, 2:55–60, 2013.
- [21] N. Lesparre, D. Gibert, J. Marteau, Y. Déclais, D. Carbone, and E. Galichet. Geophysical muon imaging: feasibility and limits. *Geophysical Journal International*, 183(3):1348–1361, 2010.
- [22] K. Nagamine. Radiography with cosmic-ray and compact accelerator muons; exploring inner-structure of large-scale objects and landforms. *Proceedings of the Japan Academy, Series B*, 92(8):265–289, 2016.
- [23] R. Sehgal, V.K.S. Kashyap, I. Kanungo, A. Saxena, A. Jain, A. Jindal, V. Singh, P. Kanavi, S.T. Sehgal, and G. Kekre. Simulations and track reconstruction for muon tomography using resistive plate chambers. In *DAE Symp. Nucl. Phys.*, volume 61, pages 1034–1035, 2016.
- [24] F. Fehr and Tomuval Collaboration. Density imaging of volcanos with atmospheric muons. In *Journal of Physics: Conference Series*, page 052019. IOP Publishing, 2012.
- [25] S. Bouteille, D. Attié, P. Baron, D. Calvet, P. Magnier, I. Mandjavidze, M. Riallot, and M. Winkler. A micromegas-based telescope for muon tomography: The watto experiment. *Nuclear Instruments and Methods in Physics Research Section A: Accelerators, Spectrometers, Detectors and Associated Equipment*, 834:223–228, 2016.
- [26] L. Oláh, H.K.M. Tanaka, T. Ohminato, and D. Varga. High-definition and low-noise muography of the sakurajima volcano with gaseous tracking detectors. *Scientific reports*, 8(1):3207, 2018.
- [27] N. Lesparre, J. Marteau, Y. Déclais, D. Gibert, B. Carlus, F. Nicollin, and B. Kergosien. Design and operation of a field telescope for cosmic ray geophysical tomography. *Geoscientific Instrumentation Methods and Data Systems*, 1:33–42, 2012.
- [28] H.K.M. Tanaka, T. Uchida, M. Tanaka, H. Shinohara, and H. Taira. Cosmic-ray muon imaging of magma in a conduit: Degassing process of satsuma iwojima volcano, japan. *Geophysical Research Letters*, 36(1), 2009.
- [29] K. Nagamine, M. Iwasaki, K. Shimomura, and K. Ishida. Method of probing inner-structure of geophysical substance with the horizontal cosmic-ray muons and possible application to volcanic eruption prediction. *Nuclear Instruments and Methods in Physics Research Section A: Accelerators, Spectrometers, Detectors and Associated Equipment*, 356(2):585 – 595, 1995.
- [30] P. Aguiar, E. Casarejos, J. Silva-Rodríguez, J.A. Vilan, and A. Iglesias. Geant4-gate simulation of a large plastic scintillator for muon radiography. *IEEE Transactions on Nuclear Science*, 62(3):1233–1238, 2015.
- [31] S.W Tang, Y.H. Yu, Y. Zhou, Z.Y. Sun, X.H. Zhang, S.T. Wang, K. Yue, L.X. Liu, F. Fang, and D. Yan. A large area plastic scintillation detector with 4-corner-readout. *Chinese Physics C*, 40(5):056001, 2016.
- [32] R. Nishiyama, S. Miyamoto, and N. Naganawa. Experimental study of source of background noise in muon radiography using emulsion film detectors. *Geoscientific Instrumentation, Methods and Data Systems*, 3(1):29–39, April 2014.
- [33] T. Kusagaya and H.K.M. Tanaka. Muographic imaging with a multi-layered telescope and its application to the study of the subsurface structure of a volcano. *Proceedings of the Japan Academy, Series B*, 91(9):501–510, 2015.

- [34] R. Nishiyama, A. Taketa, S. Miyamoto, and K. Kasahara. Monte carlo simulation for background study of geophysical inspection with cosmic-ray muons. *Geophysical Journal International*, 206(2):1039–1050, 2016.
- [35] H. Gómez, D. Gibert, C. Goy, K. Jourde, Y. Karyotakis, S. Katsanevas, J. Marteau, M. Rosas-Carbajal, and A. Tonazzo. Forward scattering effects on muon imaging. *Journal of Instrumentation*, 12(12):P12018, 2017.
- [36] Anna Pla-Dalmau, Alan D Bross, and Victor V Rykalin. Extruding plastic scintillator at fermilab. In *2003 IEEE Nuclear Science Symposium. Conference Record (IEEE Cat. No. 03CH37515)*, volume 1, pages 102–104. IEEE, 2003.
- [37] Saint-Gobain Ceramics & Plastics. *Plastic Scintillating Fibers*, 2017. Rev. 1.
- [38] Hamamatsu. *MPPCs for precision measurement*, 5 2018. Rev. 1.
- [39] A Filevich, P Bauleo, H Bianchi, J Rodriguez Martino, and G Torlasco. Spectral-directional reflectivity of tyvek immersed in water. *Nuclear Instruments and Methods in Physics Research Section A: Accelerators, Spectrometers, Detectors and Associated Equipment*, 423(1):108–118, 1999.
- [40] S. Agostinelli, J. Allison, K. Amako, J. Apostolakis, H. Araujo, P. Arce, M. Asai, D. Axen, S. Banerjee, G. Barrand, F. Behner, L. Bellagamba, J. Boudreau, L. Broglia, A. Brunengo, H. Burkhardt, S. Chauvie, J. Chuma, R. Chytracsek, G. Cooperman, G. Cosmo, P. Degtyarenko, A. Dell’Acqua, G. Depaola, D. Dietrich, R. Enami, A. Feliciello, C. Ferguson, H. Fesefeldt, G. Folger, F. Foppiano, A. Forti, S. Garelli, S. Giani, R. Giannitrapani, D. Gibin, J.J. Gómez Cadenas, I. González, G. Gracia Abril, G. Greeniaus, W. Greiner, V. Grichine, A. Grossheim, S. Guatelli, P. Gumplinger, R. Hamatsu, K. Hashimoto, H. Hasui, A. Heikkinen, A. Howard, V. Ivanchenko, A. Johnson, F.W. Jones, J. Kallenbach, N. Kanaya, M. Kawabata, Y. Kawabata, M. Kawaguti, S. Kelner, P. Kent, A. Kimura, T. Kodama, R. Kokoulin, M. Kossov, H. Kurashige, E. Lamanna, T. Lampén, V. Lara, V. Lefebure, F. Lei, M. Liendl, W. Lockman, F. Longo, S. Magni, M. Maire, E. Medernach, K. Minamimoto, P. Mora de Freitas, Y. Morita, K. Murakami, M. Nagamatu, R. Nartallo, P. Nieminen, T. Nishimura, K. Ohtsubo, M. Okamura, S. O’Neale, Y. Oohata, K. Paech, J. Perl, A. Pfeiffer, M.G. Pia, F. Ranjard, A. Rybin, S. Sadilov, E. Di Salvo, G. Santin, T. Sasaki, N. Savvas, Y. Sawada, S. Scherer, S. Sei, V. Sirotenko, D. Smith, N. Starkov, H. Stoecker, J. Sulkimo, M. Takahata, S. Tanaka, E. Tcherniaev, E. Safai Tehrani, M. Tropeano, P. Truscott, H. Uno, L. Urban, P. Urban, M. Verderi, A. Walkden, W. Wander, H. Weber, J.P. Wellisch, T. Wenaus, D.C. Williams, D. Wright, T. Yamada, H. Yoshida, and D. Zschesche. Geant4: a simulation toolkit. *Nuclear instruments and methods in physics research section A: Accelerators, Spectrometers, Detectors and Associated Equipment*, 506(3):250–303, 2003.
- [41] DG Michael, P Adamson, T Alexopoulos, WWM Allison, GJ Alner, K Anderson, C Andreopoulos, M Andrews, R Andrews, C Arroyo, et al. The magnetized steel and scintillator calorimeters of the minos experiment. *Nuclear Instruments and Methods in Physics Research Section A: Accelerators, Spectrometers, Detectors and Associated Equipment*, 596(2):190–228, 2008.
- [42] R. Calderón-Ardila. Estudio de centelladores plásticos en el proyecto mute para muongrafía de volcanes. Master thesis in geophysics, School of Physics, Universidad Industrial de Santander, Bucaramanga, Colombia, 2019.
- [43] Dieter Renker. Geiger-mode avalanche photodiodes, history, properties and problems. *Nuclear Instruments and Methods in Physics Research Section A: Accelerators, Spectrometers, Detectors and Associated Equipment*, 567(1):48–56, 2006.

- [44] Red Pitaya. Red pitaya documentation. *Release 0.97*. url: <http://redpitaya.readthedocs.io/en/latest/>(visited on 02/11/2017), 2016.
- [45] R. Calderón, H. Asorey, and L.A. Núñez. Geant4 based simulation of the water cherenkov detectors of the lagoon project. *Nuclear and Particle Physics Proceedings*, 267:424–426, 2015.
- [46] A. Etchegoyen, P. Bauleo, X. Bertou, C.B. Bonifazi, A. Filevich, M.C. Medina, D.G. Melo, A.C. Rovero, A.D. Supanitsky, and A. Tamashiro. Muon-track studies in a water cherenkov detector. *Nuclear Instruments and Methods in Physics Research Section A: Accelerators, Spectrometers, Detectors and Associated Equipment*, 545(3):602 – 612, 2005.
- [47] C Sarmiento-cano, M Suárez-Durán, A Vásquez-Ramírez, A Jaimes-Motta, R Calderón-Ardila, and J Peña-Rodríguez. Modeling the lagoon’s detectors response to secondary particles at ground level from the antarctic to mexico. In *36th International Cosmic Ray Conference (ICRC2019)*, volume 36, 2019.
- [48] D. Heck, J. Knapp, J.N. Capdevielle, G. Schatz, and T. Thouw. Corsika : A monte carlo code to simulate extensive air showers. Technical Report FZKA 6019, Forschungszentrum Karlsruhe GmbH, 1998.
- [49] L. Desorgher. MAGNETOSCOSMICS, Geant4 application for simulating the propagation of cosmic rays through the Earth magnetosphere. Technical report, Physikalisches Institut, University of Bern, Bern, Germany, 2003.
- [50] H. Asorey, S. Dasso, L.A. Núñez, Y. Pérez, C. Sarmiento-Cano, M. Suárez-Durán, and the LAGO Collaboration. The LAGO space weather program: Directional geomagnetic effects, background fluence calculations and multi-spectral data analysis. In *The 34th International Cosmic Ray Conference*, volume PoS(ICRC2015), page 142, 2015.
- [51] H. Asorey, L. A. Núñez, and M. Suárez-Durán. Preliminary results from the latin american giant observatory space weather simulation chain. *Space Weather*, 16(5):461–475, 2018.
- [52] T. Uchida, H. K.M. Tanaka, and M. Tanaka. Space saving and power efficient readout system for cosmic-ray muon radiography. *IEEE Transactions on Nuclear Science*, 56(2):448–452, 2009.
- [53] D. Gibert, F. Beauducel, Y. Déclais, N. Lesparre, J. Marteau, F. Nicollin, and A. Tarantola. Muon tomography: Plans for observations in the lesser antilles. *Earth, planets and space*, 62(2):153–165, 2010.